Meyer and Osayemwenre *International Journal of Mechanical and Materials Engineering* (2020) 15:9
https://doi.org/10.1186/s40712-020-00121-3

International Journal of Mechanical and Materials Engineering

ORIGINAL PAPER Open Access

Interfacial assessment of degraded amorphous silicon module using scanning probe microscopy

E. L. Meyer[1] and G. O. Osayemwenre[1,2*]

Abstract

This is a study of the degradation of amorphous silicon solar cells. The study accessed structural defects and the mechanical stress of solar cells at nanoscale level. Interface morphology, deformation, and internal delamination of the cells were analyzed. Adequate analysis of roughness parameters was performed to investigate the state of degradation of the amorphous silicon solar modules (a-Si:H) used in this study. Roughness parametric test is necessary in thin film solar cells production process because it is used to quantify the relationship that exists between roughness parameters and electrical efficiencies of solar cells. However, in this study, a roughness analysis was not only performed to quantify the performance of the a-Si:H module but to also compliment their mechanical degradation analysis. Roughness indicators such as root means square (RMS) roughness and average roughness were acquired from line profiles. Measurements were taken with scanning probe microscope (SPM) and PeakForce Quantitative Nanomechanical (QNM) technique was used through the cross sectional area of the analyzed samples. The method was validated with adhesive force and deformation analyses; it was established that high roughness values result from mechanical degradation. Results from the roughness parameters and the mechanical degradation analysis were further observed from in situ measurements and these showed good compatibility. The benefit of this technique is that it provides a good procedure for the evaluation of mechanical degradation without destroying any part of the intrinsic layers in a-Si:H modules.

Keywords: Surface roughness, Scanning probe microscope, Amorphous silicon solar module, Intrinsic layer, Mechanical degradation

Introduction

It is generally accepted that the performance of amorphous silicon (a-Si:H) solar cells is a function of their material properties, production designs and fabrication processes (Kabir et al. 2011). While optical properties are considered to increase the optical band gap of a-Si:H solar cells, electrical properties are considered when dealing with issues of degradation in solar cells. Oftentimes, structural properties are regarded as inherent in solar cell materials, as such, they cannot be changed. These structural properties are significantly influenced by changes in optical and electrical properties of a-Si:H solar cells as a result of degradation. In fact, changes in optical and electrical properties of a-Si:H solar cells can reasonably be attributed to changes in their mechanical properties, as opposed to it being the other way round. Hydrogenated amorphous silicon (a-Si:H) thin film has good optoelectronic properties due to its high optical absorption coefficient (> 10^5 cm^{-1}). These optoelectronic properties depend on the mechanical properties of a-Si:H materials, meanwhile, mechanical properties are affected by interface defects. In the past, less emphasis was laid on mechanical properties of photovoltaic modules because most research then was based

* Correspondence: gosayemwenre@ufh.ac.za
[1]Fort Hare Institute of Technology (FHIT), Alice, Eastern Cape, South Africa
[2]Department of Physics, University of Fort Hare, Alice 5700, South Africa

Springer Open

© The Author(s). 2020 **Open Access** This article is licensed under a Creative Commons Attribution 4.0 International License, which permits use, sharing, adaptation, distribution and reproduction in any medium or format, as long as you give appropriate credit to the original author(s) and the source, provide a link to the Creative Commons licence, and indicate if changes were made. The images or other third party material in this article are included in the article's Creative Commons licence, unless indicated otherwise in a credit line to the material. If material is not included in the article's Creative Commons licence and your intended use is not permitted by statutory regulation or exceeds the permitted use, you will need to obtain permission directly from the copyright holder. To view a copy of this licence, visit http://creativecommons.org/licenses/by/4.0/.

on crystalline silicon solar modules which are believed to be less prone to mechanical defects. However, since the last decade, attention has shifted to thin films and perovskite solar cells. Hence, the need to concentrate on the mechanical properties of a-Si:H solar cells and their associative features, such as, interface roughness and delamination. Therefore, in this study, focus is on the changes that occur in interface layers roughness as it has a negative impact on the electrical output of amorphous solar cells (Prastani 2015; Su et al. 2003). Consequently, this paper deals with the micro-structural, defects, and mechanical properties of amorphous silicon solar cells. Firstly, it aims to determine which region of the module is more prone to mechanical degradation and compare the mechanical properties of the defective with the non-defective regions of the module. It also intends to establish if there is any direct relationship between interface roughness and mechanical degradation. This work, quantifies mechanical degradation by the degree of decrease of adhesive force and interlayer delamination in the form of deformation. While roughness in this sense is not the usual surface morphological roughness, but the change in the smoothness of the interface of the different layers that constitutes the active region of the a-Si:H module. The degradation of mechanical properties which results in mechanical defects can be observed as micro-structural defects when the active region of an a-Si:H module is mapped with atomic force microscope (AFM). The belief is that such micro-structural defects are inherent in the substrate of such solar cells during their manufacturing processes, although there are very few scientific reports to support this claim (Su et al. 2003). Nevertheless, as the module starts to degrade, more its micro-defects start to increase; hence, the roughness in its defective region is expected to be more pronounced than the one from the non-defective (hotspot) region. One of the motivations for this study is the desire to acquire sufficient information on the correlation between the micro-structural defects and the performance degradation of a-Si:H modules. Mechanical property variation at nanoscale level has a way of initiating stresses or damage to the photovoltaic (PV) material, and this can potentially result in premature failure of PV modules. Thus, to improve the reliability of the amorphous silicon solar cells, it is essential to increase their layers mechanical strengthen. Therefore, set a mechanical limit that can reduce the cost of production (Popovich 2013) and have a detailed comprehension of the degradation of mechanical properties. The results presented hereunder provides a deeper understanding of the mechanical properties of the a-Si:H modules.

Materials and methods

The validation process

Some regions of a delaminated single junction amorphous silicon (a-Si:H) module was cleaved, contact fabrication was performed on them, and measurements were taken in a relatively isolated room that was free from acoustic noise. The cleaving of the samples was done after they were placed in a nitrogen refrigerator to aid the final cutting process. The initial delaminated sample had an area of 6 cm^2 while the area of interest was 2 cm^2. This formed part of the quality control process observed in this study. It was also crucial to obtain a small part of the a-Si:H module which was scanned with the scanning probe microscope (SPM) in the laboratory. The purpose of this aspect of the experiment was to try to validate the possibility of the SPM to perform in situ measurements without destroying the active layers of a-Si:H module during defects investigation.

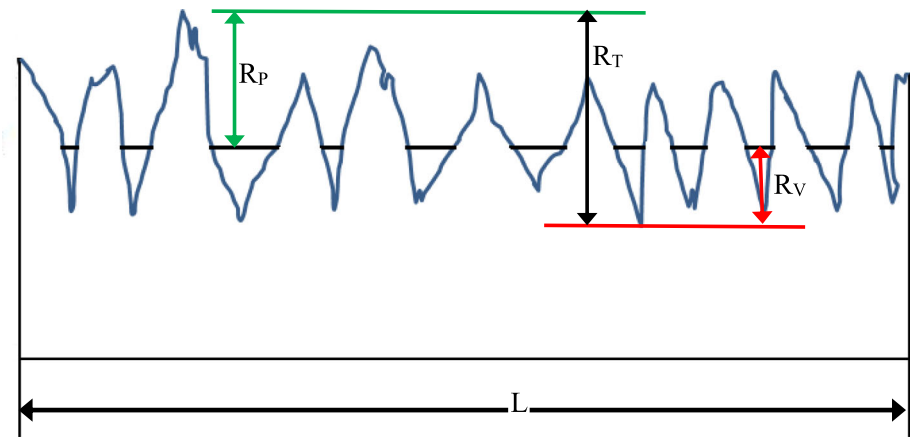

Fig. 1 Schematic illustration depicting high spot count and low spot count for the determination of peak and surface roughness (adapted from Park, 2011).

The steps taken in the aforementioned process include the following:

- Defective and non-defective regions of 6 cm^2 each were identified on a large module of 30 × 93 cm^2
- The regions of interest (2 cm^2) were selected on a large sample (6 cm^2)
- The region of interest was cleaved and taken to the laboratory that was isolated from noise and vibration
- Sub-regions were obtained from the aforementioned (2 cm^2) region of interest using the SPM in AFM mode for portable configuration
- Non-contact mode was used to scan all the a-Si:H samples and the mechanical and roughness results of the defective and non-defective regions were compared

Statistical analysis of samples roughness

Root mean square (RMS) roughness is a useful statistical tool for describing the roughness of the surface of a material. In this study, statistical analyses were performed on the images acquired from both the defective and non-defective regions. The effects of degradation on the cross-sectional area of the a-Si:H samples were examined by analysing different regions on both the defective and non-defective samples. The AFM images of the samples showed some differences between their surface roughness and vertical heights. In addition, some quantitative information about the effect of degradation as they relate to defects on the topography of the inter-layer of the samples were derived Fig. 1 describes some parameters used in the statistical analysis; this is important since the scale on the topography image only provides general information about roughness without stating how the various points and locations in the various layers changed when they were approached by the sharp tip of the cantilever. The position and definition of profile peak height (Rp), profile maximum height (R_T), and profile valley depth (Rv) are illustrated in Fig. 1

Procedure for performing roughness and amplitude parameters analysis (peak and valley)

The height sensor bar is measured from the AFM image; it indicates the highest height sensor (topography) and the lowest height sensor of the entire scanned sample (Voigtländer 2015; Oliver and Pharr 2004). Therefore, it is not the best way to illustrate topographical variation across the cross section of the surface of a material since defects on morphological surface are of utmost importance in this kind of analysis (Dunford 2013; Sahay and Ghosh 2018). Roughness across the various layers was calculated from arithmetic average of the heights sensor through various parameters.

The sensitive nature of the interfaces of the a-Si:H layer necessitated the choice of non-contact mode in scanning the samples. Theoretically, the AFM mode employed depends on the surface characteristics of a sample's material and how hard/sticky the sample is. The contact mode is mostly useful for hard surfaces where a tip is in contact with a surface. But to avoid contamination of a material on a surface, the non-contact mode is preferred. Excessive force in the contact mode can damage the surface or blunt the probe tip. The only challenge in this non-contact mode is its high sensitivity to external vibrations and issues with tip to sample engagement and retraction of tips. The statistical analysis of surface roughness is normally done via roughness average (Ra) and root mean square (RMS). Equation (1) defines surface roughness average (Park 2011).

$$\mathrm{R_a} = \frac{1}{L}\int_0^L |Z(x)|\mathrm{dx} \tag{1}$$

Where $Z(x)$ and L are the surface profile describing the function expressed in terms of height (Z) and the position (x) and the length of the sample being analysed respectively. The root mean square roughness is similar to the average roughness, since RMS (R_q) is the absolute mean square of the surface roughness (De Oliveira et al. 2012). Therefore, the R_q value depends on the size of sample scanned and it is more sensitive in analysing peaks and valleys compared to Ra, as defined by Eq. 2 (Gadelmawla et al. 2002). The differences between peak height, valley depth, and maximum profile height illustrated in Fig. 1 are defined by Eqs. 3, 4, and 5, respectively.

$$\mathrm{R_q} = \mathrm{RMS} = \sqrt{\frac{1}{2}\int_0^L \left|Z^2(x)\right| \, dx} \tag{2}$$

$$R_\mathrm{p} = |\mathrm{maxZ(x)}| \text{ for } 0 \le x \le L \tag{3}$$

$$R_\mathrm{v} = |\mathrm{maxZ(x)}| \text{ for } 0 \le x \le L \tag{4}$$

$$R_\mathrm{T} = \mathrm{Rp} + R_\mathrm{V} \tag{5}$$

where R_a is roughness average, R_q is root mean square (RMS) roughness, R_T is maximum height of the profile, R_v is maximum profile valley depth, and R_p is maximum profile peak height. A statistical analysis of the different parameters is presented below. It includes the root mean square roughness (RMS or R_q), mean height roughness

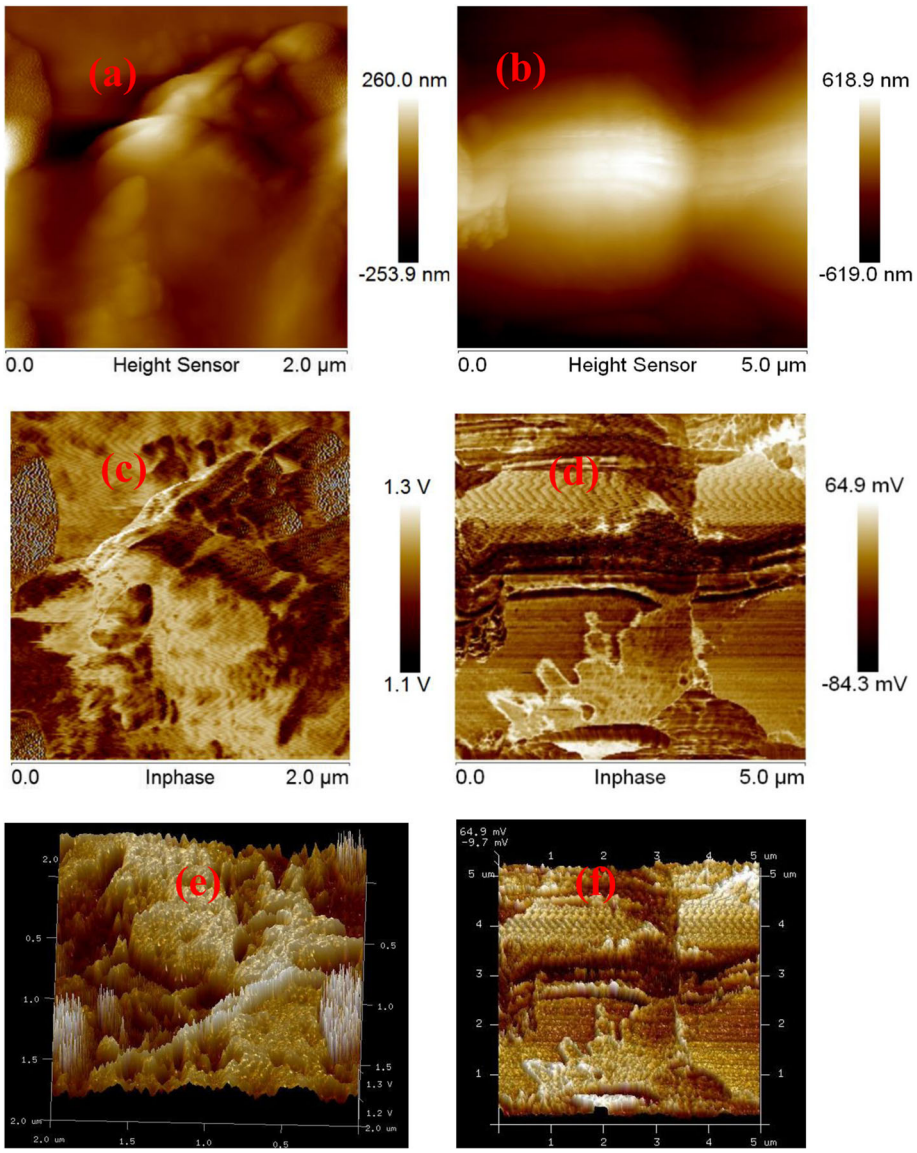

Fig. 2 Height sensors for the non-defective sample (**a**) and defective sample (**b**). Inphases of the following: non-defective sample (**c**) and defective sample (**d**); non-defective and defective samples inphase 3D images respectively

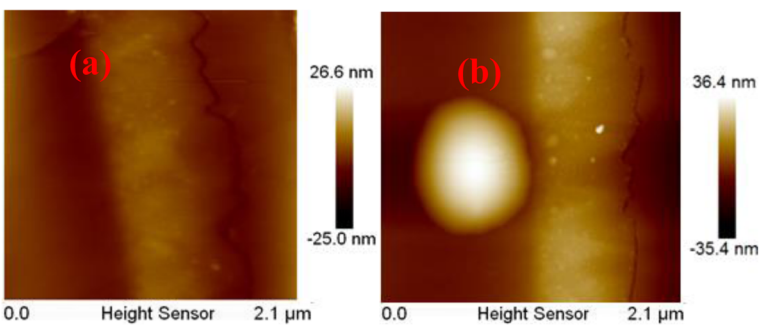

Fig. 3 Topography images of the samples from the : (**a**) non defective and (**b**) defective region

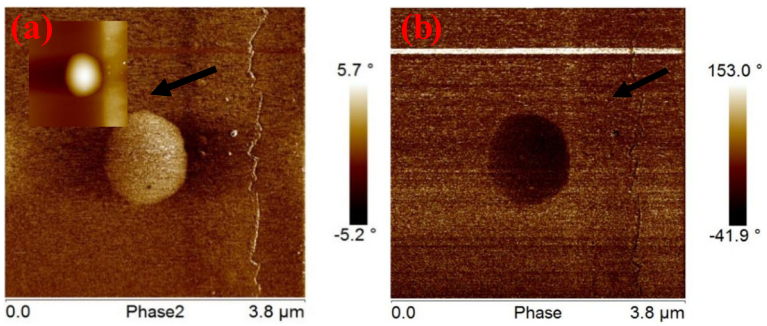

Fig. 4 Defective samples: (**a**) phase images, (**b**) phase image, at different mapping angle at set-point amplitude of $A/A_0 = 0.75$

(R_a), and arithmetic average absolute values for the height deviations. Every calculation was done with reference to the Z_i deviation, which is the mean plane of the surface.

Results and discussion

Inphase and phase as tools for mechanical analysis

The instrument used in this study is a special ICON scanning probe microscopy (ICON-SPM). This system has a PeakForce tapping mode as a standard option, unlike the SPM previously used by researchers. The ICON-SPM has more scanning modes, such as the contact mode, the non-contact mode, and the tapping mode. In PeakForce tapping mode, the system exhibits a sinusoidal signal with the probing tip undergoing up and down vibrations. With the aid of a lock-in amplifier, the inphase and quadrature which are the '*x*' and '*y*' outputs, respectively, are acquired. A similar output known as 'phase' is also obtained from the AFM tapping mode (Saive 2014). This phase has a direct physical meaning; this makes it different from the inphase obtained from the PeakForce Quantitative Nanomechanical (QNM) which has no direct physical meaning. The topographical images of samples from the defective and non-defective regions are presented in Fig. 2. The sample from the defective region is presented in Fig. 2b, and it has a size (scale) that is different from the non-defective sample presented in Fig. 2a. In addition, the height sensor and the inphase for both the defective and non-defective regions are indicated in Fig. 2a–d, respectively. While the scanned area for the defective region was 2 µm × 2 µm, that of the non-defective sample was 5 µm × 5 µm. Although a direct physical interpretation of defect could not be derived from inphase images but such images helped to effectively monitor the adhesive force to know if the structural change was due to defects or from different substrates which differ from the analysed a-Si:H samples. In the 3D images in Fig. 2e,f. Fig. 2e appears to have a larger grain than Fig. 2f; this may be due to the higher potential difference and sample-tip indentation resulting from the AFM tip.

PeakForce QNM inphase and quadrature is mainly used to identify changes in the material properties of solar cells; hence, it was used in this work. Although its tapping mode phase is similar to its inphase, it reveals more about the distribution of various components in the doped solar cell than the inphase. Nevertheless, when the PeakForce QNM is well calibrated, it can provide useful information about mechanical properties required for material characterisation

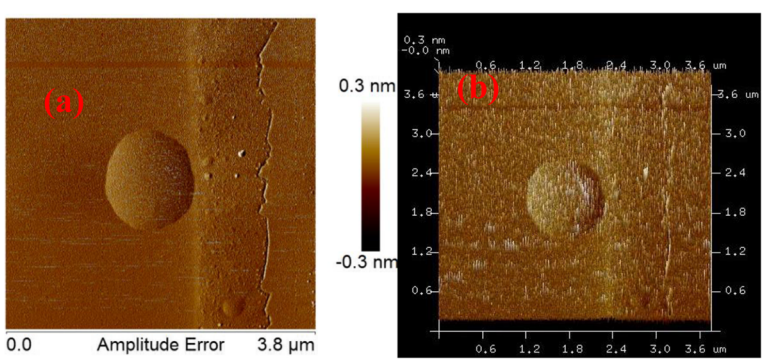

Fig. 5 Quantification of average amplitude error with PFQNM measurement in (**a**) 2 D image, (**b**) 3 D image

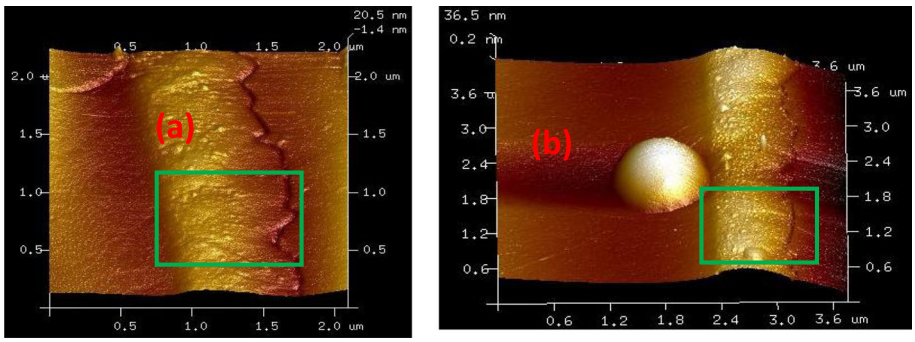

Fig. 6 3D images of the topographies for the non-defective sample (**a**) and the defective region of the non-defective (**b**) sample

such as adhesion, Young's modulus, and deformation. Hence, the inhomogeneity in the regions of the samples can be investigated and correlated with changes in the defect levels. In plain terms, the lock-in amplitude produces two kinds of outputs described by R$\cos(\boldsymbol{\theta})$ (inphase) and *R*$\sin(\boldsymbol{\theta})$ (quadrature); these outputs are acquired when the system oscillates in a frequency different from the cantilever resonance frequency (Saive 2014; Drijkoningen et al. 2014). Therefore, the PeakForce QNM was used to monitor the difference between the material properties of the samples from the defective and non-defective regions.

PeakForce QNM as a tool for mechanical properties analysis

In the preliminary part of this study, the amplified lock-in feedback was used to check the degree of authenticity of the results. Nonetheless, it is necessary to ensure that the results of the measurements are accurate by crosschecking the output of the lock-in amplifier. The changes in the mechanical properties at the cross-sectional areas of the samples were measured using PeakForce QNM. A nitride doped silicon probe cantilever (SNL-D, Brusker, USA) of spring constant k = 1.2 was used in this study. Though most authors use lower spring constants, those kinds of constants make it difficult to measure topographies. With the spring constant used in this study, both topography imaging and lock-in amplifier outputs were measured simultaneously. These outcomes are reasonable, considering the high resolution of the tip-force interaction in the PFQNM mode. Figure 3 presents the topography of 2.1 μm × 2.1 μm for both the defective and non-defective samples.

To further examine the moon-like defect seen in the defective region, a large area of 3.8 μm × 3.8 μm is scanned from the defective sample and this is shown in Fig. 4. The inserted monogram in Fig. 4a is the same as Fig. 3b image.

Figure 4a,b shows the non-contact (nC) mode phase image of the sample from the defective region of a-Si: H module. The circular features seen in both the height and phase images are blister clusters which occurred as a result of thermal stress. However, the crack vertical line which runs from top to bottom in Figs. 3b and 4 corresponds with the intrinsic layer and the interface is clearly shown. In Fig. 4a, the

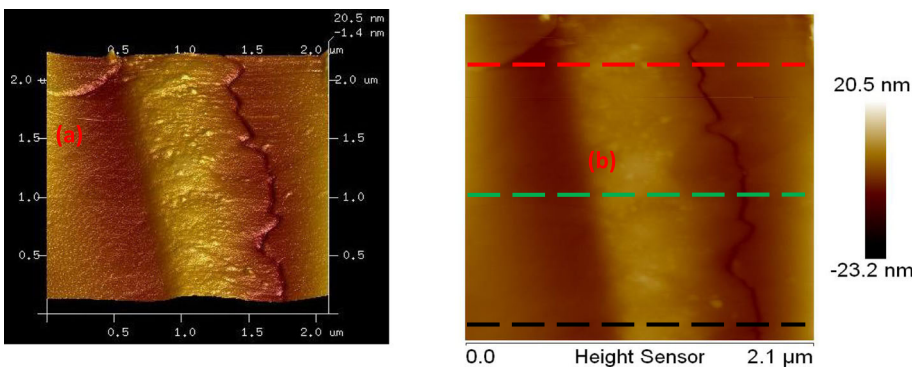

Fig. 7 Non-defective sample image in (**a**) 3D and, (**b**) 2D

Table 1 Statistical parameters of the non-defective sample

Horizontal distance (μm)	Vertical distance (nm)	Surface distance (μm)	*R*max *R*a (nm)	RMS *R*q (nm)	Ave. height (Ra)(nm)	*Radius* (μm)	*Radius sigma* (μm)
0.116	1.189	0.317	8. 63	1.227	9.17	*4.035*	*0.001*
0.120	3.917	0.421	7.29	0.447	8.511	*7.098*	*0.685*
0.116	7.016	0.3 17	7.16	1.238	4.890	*5.933*	*0.825*

height sensor image of the defective sample is inserted while the entire Fig. 4a,b present the phase images at different phase angle (Voigtländer 2015; Oliver and Pharr 2004). The height and phase images show similar structural features that can be used to identify defect locations in the mapped samples. The horizontal lines indicated by dark arrows in both phase images in Fig. 4a,b do not indicate a rise in heights but indentation artefacts (Knoll et al. 2002). Details of indentation artefacts can be found in Erike Christian's work. This phenomenon can be linked to the nature of the cantilever used (Melitz et al. 2011; Barbet et al. 2014). The results presented in this work reveal that line of indentation artefacts are peculiar to phase images; hence, their absence in the height images. Therefore, the occurrence of indentation does not have any concrete physical meanings. Indentation artefacts are severe in the region marked with arrow as seen Fig. 4. The fact that this line also appears in Fig. 5 and absent in Fig. 3 implies the factures are induced; hence, there is no proof that it is a defect. Meanwhile, the use of a setpoint of 0.75 in the analysis may also contribute to this observation. To check the integrity of the identified defect spot, a qualitative system error measurement was done, the data collected was analysed and the resulting microgram is displaced in Fig. 5. Figure 5a is the 2D error image while the 3D error image is presented in Fig. 5b.

The low amplitude error recorded for this measurement, as shown in Fig. 5, connotes a high level of accuracy due to good communication signal between the instrument and the calibration. In Fig. 6, the region of interest, which encompasses the active region, is indicated by a green box for the non-defective and defective sample in Fig. 6a,b respectively.

Statistical analysis

Figure 6 presents the 3D images of both the non-defective and defective of the a-Si:H samples; the active region is indicated by the green box. These images help to visualize the cross-sectional area of the active region. The investigation of the smoothness and topography across the interface of the non-defective sample is represented with Fig. 7. From this result, the absolute spatial dimension of the cross-sectional area of the sample is observed. The 3D image in Fig. 7 shows slight variations and detailed features of the samples structure. The roughness in terms of the root mean square (RMS) and the average roughness previously defined were calculated. The calculated value for the maximum RMS and average roughness are presented in Table 1 below. In Table 1, the measured parameters are written in black, while the parameters in red are constant derivatives obtained after system calibration. The positions where the lines profile for the non-defective sample were taken are indicated in Fig. 7b while the color code helps to link Fig. 7b with Fig. 8a. The intrinsic part of the image and the deep gaps between successive peaks are seen in the lines profile in Fig. 8 as indicated with color codes; such detail could not have

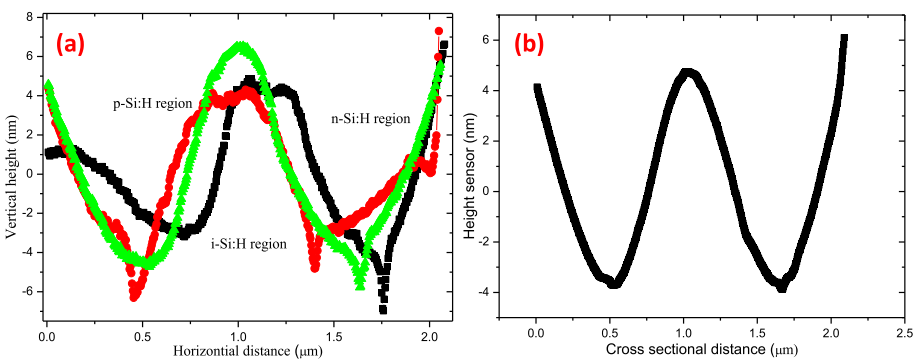

Fig. 8 Line profile of topography from the non-defective sample (**a**) and the net profile acquired from three lines (**b**)

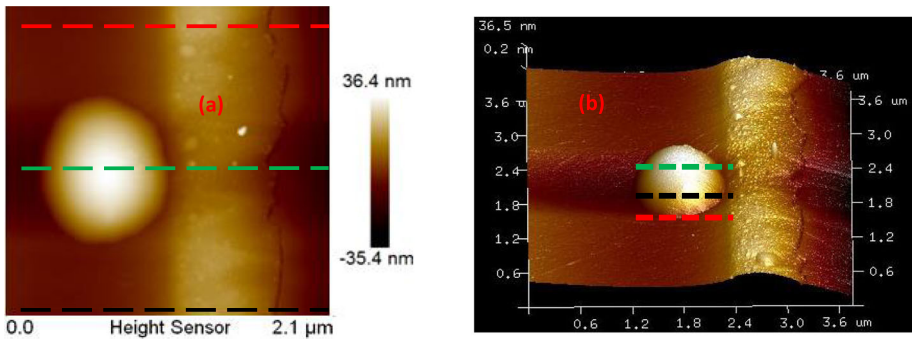

Fig. 9 Topography of the defective sample: **a** 2.1 μm × 2.1 μm, 2D image, and **b** 3.6 μm × 3.6 μm, 3D image with 3 lines across defective cluster

been visible without line profile analysis. The maximum value of the RMS and average roughness are 1.23 nm and 8.63 nm, respectively. From Fig. 8, the total topography graph is presented in (b) while (a) shows the three lines marked in Fig. 7b. The choice of these line positions is based on their high roughness when compared to the other regions. This further buttresses the importance of statistical analysis at nanoscale level because roughness data, as acquired, does not make room for point-point depth analysis of the material topography. It is noteworthy that Fig. 7b is the same as Fig. 8a; however, in addition to its height sensor, it indicates the location used for calculating the interface roughness.

To further investigate interface roughness, statistical analysis of various parameters was performed using statistical tools. The result for the non-defective sample is presented in the table below. On the other hand, Fig. 9 shows SPM images of the defective sample in 2D and 3D respectively.

To compare the results of the defective and the non-defective samples, a statistical analysis was performed for the defective sample. The position of the line profile used for the analysis is shown in Fig. 9 above. It is noteworthy that Fig. 9 a is the same as Fig. 3b above; however, it indicates the line profile used for the analysis presented in Table 3. The defective sample was analyzed as the non-defective sample, and an area measured 2.1 μm × 2.1 μm was investigated for the defective sample as illustrated in Fig. 9a. Three lines were drawn and plotted to compare the surface morphologies. The acquired data for both samples were obtained at the spectral parameters given in Table 2. The spectral parameters were found to be different for both samples even though the same calibration was maintained throughout the measurements. These measurement conditions needed to be adhered to for the reproducibility of the experiment. Thus, to estimate the actual roughness of the morphologies of the samples, root mean square (*R*q) and average cross-sectional area roughness (*R*a) were calculated for the three-line profiles shown in Fig. 9a. The calculated values and some measured parameters of the samples are presented in Table 3. It is important to note that the same calibration was used for the defective and non-defective samples as earlier mentioned. More so, the maximum value of the *R*q and *R*a of the defective sample are 19.184 nm and 4.843 nm, respectively.

The image of the defect cluster observed in the defective sample was analyzed with three line colors as indicated in Fig. 9b. In order to estimate the average topography of this spot, the room mean square (RMS) and average roughness (Ra) were calculated. The RMS and *R*a (max) calculated value are 9.683 nm and 10.035 nm, respectively; these values are quite high compared to values obtained from their neighbouring regions. The high value obtained for the average roughness (*R*a) of the defect cluster which is observed to be more than that of the *R*a of the defective sample is as a result of the reduced cross-sectional area and similar phase value of the defective sample. A line profile through the medium of the defect cluster is plotted in Fig. 10a below, while Fig. 10b presents the graph of the three lines used for the roughness analysis of the defect

Table 2 PFQNM measured spectral parameters observed during measurements

Sample	Spectral period (μm)	Spectral frequency (μm)	Temporal frequency(Hz)	Spectral RMS amplitude (nm)
Non-defective	1.05	0.957	25.9	2.56
Defective	0.331	3.35	2.80	0.0825

Table 3 Statistical analysis of the defective sample

Horizontal distance (μm)	Vertical distance (nm)	Surface distance (μm)	*R*max *R*a (nm)	RMS *R*q (nm)	Average height (*R*a)(nm)	Radius (nm)	Radius sigma (nm)
0.516	9.022	0.517	19.184	4.843	2.910	9.417	0.227
0.516	10.790	0.517	17.212	2.939	3.939	3.310	0.003
0.520	6.753	0.521	7.778	2.098	2.580	6.765	0.471

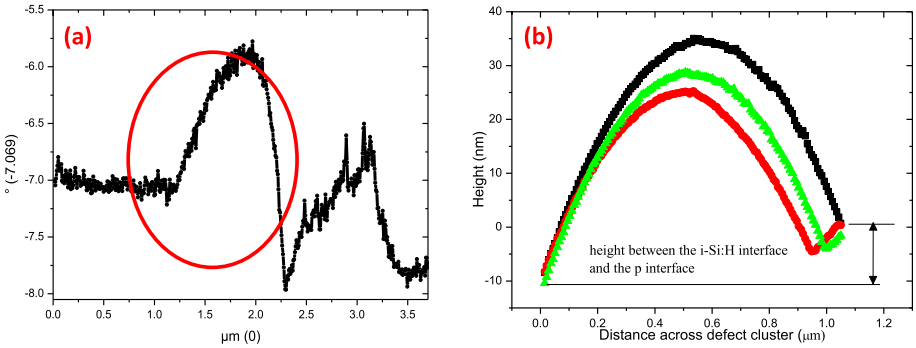

Fig. 10 Line profile across the circular defective cluster, observed from the defective sample: **a** line profile through the middle of the defect cluster and **b** three lines across the defect cluster as indicated in Fig. 9b used for the calculation of RMS and *Ra*.

cluster. It is important to note that the position of the defect cluster is indicated by the red circle in Fig. 10a. This circular defect cluster is best visualized from a PFQNM image. Hence, Fig. 11a,b below shows the phase images of the defective sample with different phase values. The position of the cluster and the deformation effect of the cluster in different phases are clearly seen.

In Fig. 10b, the difference in the curves at the right side of the graph is due to the presence of an interface, which has an *R*v value that is different from the average surface value of the image. This also shows how important such analysis is, because such defects are close to recombination centers and can act as trap centers for shallow defects. Detail analysis of this region is presented in Table 4 and more information about the defective region is presented in "PeakForce Quantitative Nanomechanical analysis of the defective cluster" section.

To verify the authenticity of the measurement, the phase image of the amplitude error was checked, and an error amplitude of − 3 nm was recorded as presented in Fig. 4 above; this value is reasonable for a measurement of this kind.

PeakForce Quantitative Nanomechanical analysis of the defective cluster

An analysis of the scanned area of the defective sample was done below the initial position observed in Fig. 9; the purpose was to ensure that the acquired images cut across the defective cluster. This act made it possible to visualize what was behind the cluster. The importance of these image mappings is that they provide a derivative insight into the cluster, and this is seen as a hole in Fig. 12b,d. Thus, it can be said that this blister-like defect is an accumulation of defects, which is probably due to thermal induced precipitation and migration of particles. The accuracy of these mappings can be seen in the image of the amplitude error presented in Fig. 12e below. It only has a peak height of 3 nm (*R*p) and a peak valley (*R*v) of − 7 nm. Below are the derivative images obtained from PFQNM and they include phase, quadrature, and error image.

Figure 12a–f shows the PFQNM quandrature, phase, and error amplitude of a section of the defective sample. The results presented in Tables 1, 2 and 3 are the average values for both measurements from the defective and non-defective samples. These results are justified by the fact that calibrations were constant throughout the

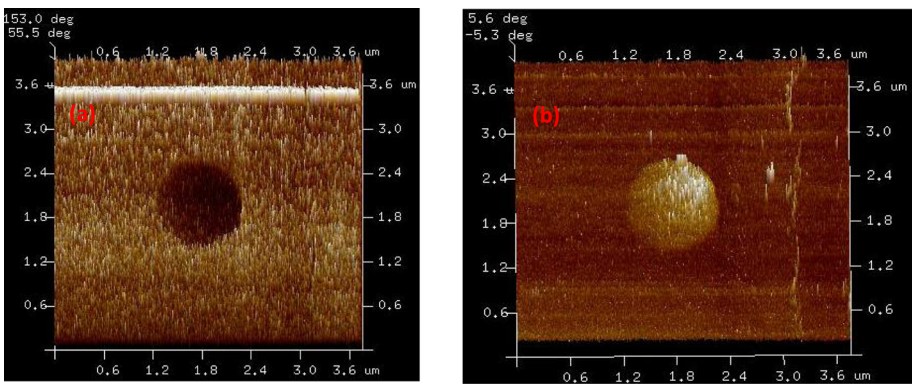

Fig. 11 PFQNM image for the defective sample in different phases

Table 4 Statistical analysis for the blister defective cluster

Horizontal distance (μm)	Vertical distance (nm)	Surface distance (μm)	*R*max Ra (nm)	RMS *R*q (nm)	Average height (*R*a)(nm)	Radius (nm)	Radius sigma (nm)
0.265	12.731	0.265	9.971	9.683	9.880	3.625	0.136
0.221	10.613	0.221	11.515	7.322	7.296	3.878	0.102
0.258	10.494	0.258	10.173	9.244	10.035	3.435	0.137

measurements. However, the resulting images of their inphase and phase measurements do not have direct correlation with the images of their tapping mode phases, but they have significant influence on the mechanical properties of the samples (Barroso-Bujans et al. 2009). A useful imaging technique that can be used for physical interpretation is the phase image from the AFM tapping mode (Maturova et al. 2009). Although it cannot be used directly in most cases, such as when the right mechanical calibration of the specific sample to be characterized has not been done and proven accurate. In this section, only

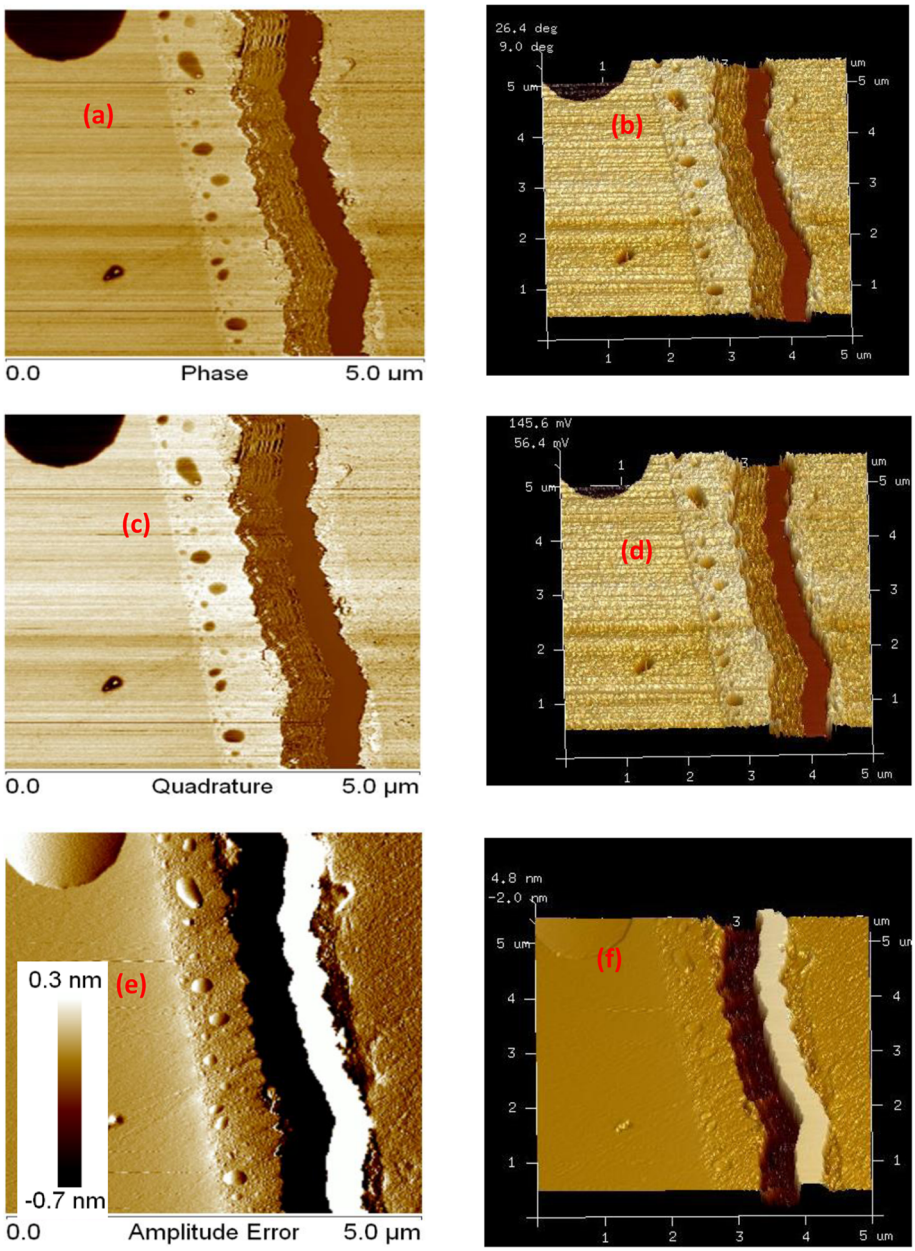

Fig. 12 PFQNM phase derivative images taken from the defective region (**a-b**); 2D and 3D phase images (**c-d**); 2D and 3D quadrature images (**e-f**); 2D and 3D images of the measured amplitude error

results from the defective sample are analyzed and presented. This is because of the similarities between the phase images taken with the PFQNM and the phase images of the non-defective sample. In the case of the defective sample, more insight is shown from the PFQNM image, whereas, this is invisible from the AFM imaging. Importantly, a significant change or reduction in these results could have reduced the lifetime of the antireflective film in the region of the module where the samples were taken. These kinds of changes could occur because of water ingress adsorption in the encapsulation layer of degraded a-Si:H modules which influence layers' degradation (Osayemwenre et al. 2017).

Conclusion

This research is a comparative study of several statistical parameters obtained using SPM and QNM instruments for interface defects analysis. This study has revealed the need to employ other interface roughness parameters to access the mechanical properties of a-Si:H modules by using all the dynamic AFM modes which can properly represent the material properties of solar modules. Some of these AFM modes include in phase, phase, quadrature, and DMT modules; however, they cannot be solely and conclusively used to represent the mechanical properties of analyzed samples. Notwithstanding, the AFM is one characterization technique that can be used to substantiate the variation and quality of a-Si:H materials. The results presented in this paper demonstrate that SPM and PQNM are useful tools for accessing micro-defects and their profiles in a-Si:H modules.

Acknowledgements

The authors disclose receipt of financial support for this research, authorship, and/or publication of this article. We are grateful for the financial support from our sponsors: South African National Research Foundation (NRF) and Govani Beki Research & Development Centre (GMRDC) of the University of Fort Hare.

Authors' contributions

The work is carried out by the corresponding author GO. All authors read and approved the final manuscript.

Funding

I have no funding sources to declare.

Availability of data and materials

All data are included within the text of the document. Hence, there are no separate data files.

Competing interests

The authors declare that they have no competing interests.

Received: 30 April 2020 Accepted: 18 August 2020
Published online: 03 December 2020

References

Barbet, S., Popoff, M., Diesinger, H., Deresmes, D., Théron, D., & Mélin, T. (2014). Cross-talk artefacts in Kelvin probe force microscopy imaging: A comprehensive study. *Journal of Applied Physics*, *115*(14), 144–313.

Barroso-Bujans, F., et al. (2009). Grafting of poly (acrylic acid) onto an aluminum surface. *Langmuir*, *25*(16), 9094–9100. https://doi.org/10.1021/la900518s.

R.R.L. De Oliveira, D.A.C. Albuquerque, T.G.S. Cruz, F. M. Yamaji and F. L. Leite (2012). Measurement of the nanoscale roughness by atomic force microscopy: basic principles and applications, atomic force microscopy - imaging, measuring and manipulating surfaces at the atomic scale, Dr. Victor Bellitto (Ed.), ISBN: 978-953-51-0414-8.

Drijkoningen, J., Kesters, J., Vangerven, T., Bourgeois, E. (2014). Investigating the role of efficiency enhancing interlayers for bulk heterojunction solar cells by scanning probe microscopy. *Organic Electronics*, *15*(6),1282–1289.

Dunford, A (2013). Friction and the texture of aggregate particles used in the road surface course, Thesis submitted to the University of Nottingham for the degree of Doctor of Philosophy.

Gadelmawla, E.S., Koura, M.M., Maksoud, T.M.A., Elewa, I.M., Soliman, H.H. (2002). Roughness Parameters, Journal of Materials Processing Technology, Vol. 123, No 1,(apr. 2002), pp. 133-145, 0924-0135.

Kabir, M. I., Amin, N., Zaharim, A., and Sopian, K. (2011). Effect of energy bandgap of the amorphous silicon carbide (A-Sic:H) layers on A-Si multijunction solar cells from numerical analysis. Proceedings of the 8th WSEAS Int. conf. on non-linear analysis, non-linear systems and chaos.

Knoll, A., Horvat, K. S., Lyakhova, G., Krausch, G., Sevink, J. A., Zvelindovsky, A. V., & Magerle, R. (2002). Phase behavior in thin films of cylinderforming block copolymers. *Physical Review Letters*, *89*, 035501.

Maturova, K., Kemerink, M., Wienk M. M., Charrier, D. S. H., Janssen, R. A. J. (2009) Scanning Kelvin probe microscopy on bulk heterojunction polymer blends. Advanced Functional Materials., 19(9): 1379–1386, http://dx.doi.org/https://doi.org/10.1002/adfm.200801283.

Melitz, W. et al., (2011). Surface Science Reports Kelvin probe force microscopy and its application, Surface Science Reports. Elsevier B, 66(1): 1–27, doi: https://doi.org/10.1016/j.surfrep.2010.10.001.

Oliver, W. C., & Pharr, G. M. (2004). Measurement of hardness and elastic modulus by instrumented indentation, advances in understanding and refinements to methodology. *Journal of Materials Research*, *19*(3), 2004.

Osayemwenre, G. O., Meyer, E. L., Taziwa, R. T., & Mamphweli, S. N. (2017). Photothermal degradation of degraded a-Si:H. *Ovonic Research Journal*, *10*(6), 421–444.

Park Systems. Accessed 10; 03; 2011. Available from <http://www.parkafm.co.kr/>.

Popovich, V. (2013). Microstructure and mechanical aspects of multicrystalline silicon solar cells," Submitted at Delft University of Technology for the partial fulfilment of the degree of doctor of Engineering. Thesis.

Prastani, C. (2015). SnS nanoparticles to boost CuInS2 solar cells. Nanophotonics-Physics of Devices group, at Debye Institute for Nanomaterials Science at Utrecht University.

Sahay, C and Ghosh, S (2018). Understanding surface quality: beyond average roughness (Ra), American Society for Engineering Education, ASEE Annual conference & Exposition.

Saive, R (2014). Thesis submitted to faculty for the natural science and for mathematics. At University of Ruperto-Carola University of Heidelberg for the degree of doctor of natural science. Thesis.

Su, C., Huang, L., Neilson, P., and Kelley, V. (2003). In-situ measurements of in plane and out-of-plane force gradient with a torsional resonance mode afm. Proc. 12th Int. Conf. on Scanning Tunnelling Microscopy/Spectroscopy and Related Techniques. 349-352.

Voigtländer, B. (2015). Scanning probe microscopy: atomic force microscopy and scanning tunneling microscopy, Springer superstrate nanocrystalline silicon solar cell. *Digest Journal of Nanomaterials and Biostructures*, *8*, 573–579.

Publisher's Note

Springer Nature remains neutral with regard to jurisdictional claims in published maps and institutional affiliations.